final size distribution (a mode radius of about 0.4 μm) the fractal aerosol absorbs more strongly than equivalent spheres by a factor of 4 to 5.

Soot is the key absorber in the post-nuclear-war atmosphere, and because soot particles occur not as spheres but as fractal aggregates with a dimension less than 2, a realistic assessment of nuclear-winter effects requires that the optical consequences of the fractality of soot be taken into account. The central question is how much of the smoke in a post-nuclear-war atmosphere would exist as fractal clusters.

Sooty smoke initially provides about half of the post-war optical depth[5], but ageing may change this proportion. Upon contact with water vapour some smoke particles will act as nuclei for cloud condensation (CCN). Sooty smoke particles may collapse under such cloud-processing into compact structures more appropriately modelled as spheres (G. W. Mulholland, unpublished results). Although the fraction of soot particles likely to be processed in this way is not known—and so far soot appears reluctant to form CCNs[17]—the effect will be to reduce the relative proportion of fractal smoke. On the other hand, oily smoke particles form CCNs much more readily than does sooty smoke[17] and so are more likely to rain out; and fractals fall more slowly under gravity, on account of the greater atmospheric drag[18]. Both of these effects will enhance the proportion of fractal soot in the smoke, in contrast to the cloud-processing effect.

The results presented above indicate that the absorptivity of fractal sooty smoke is underestimated whenever it is modelled as a distribution of spheres whose mode radius exceeds 0.1 μm. Recent studies of the climatic effects of nuclear war are based on spherical smoke particles of mode radii from 0.2 to 0.4 μm (refs 3, 7). According to the study of Ghan *et al.*[3], 'uncoagulated' smoke (spheres of mode radius 0.1 μm) causes a fall in temperature in the mid-Northern hemisphere after 20–30 days that is some 5–10 °C greater than that caused by the 'coagulated' smoke (spheres of mode radius 0.4 μm) of their baseline study. Fractal smoke absorbs about as strongly as their 'uncoagulated' smoke. Therefore, unless the collapse resulting from cloud-processing is complete, so that none of the smoke produced remains fractal, their baseline study underestimates the severity of nuclear winter.

If it is valid to assume that soot provides half the optical depth, and we incorporate fractality approximately by setting soot absorptivity as constant at its measured value, the short-term effect of soot fractality is to make the nuclear winter colder by several (up to 5) degrees. Its long-term effect could be a doubling or trebling in the opacity of the residual smoke layer that is believed to stabilize in the upper atmosphere. Both effects are very significant in biological and climatic terms. They warrant further investigation of the morphology and cloud-nucleating capacity of smoke, and a serious treatment of smoke fractality in nuclear-winter simulations. □

Received 15 December 1988; accepted 9 May 1989.

1. Schneider, S. H. & Thompson, S. L. *Nature* **333,** 221–227 (1988).
2. Turco, R. P. & Golitsyn, G. S. *Environment* **30**(5), 8–16 (1988).
3. Ghan, S. J. *et al. J. geophys. Res.* **93,** 8315–8337 (1988).
4. Berry, M. V. & Percival I. C. *Optica Acta* **33,** 571–589 (1986).
5. Penner, J. E. *Nature* **324,** 222–226 (1986).
6. Radke, L. F. *et al.* in *Proc. Third WMO Scientific Conf. on Weather Modification*, World Meteorological Organisation, Geneva, 119–126 (1980).
7. Thompson, S. L. *et al. J. geophys. Res.* **92,** 10942–10960 (1987).
8. Penner, J. E. & Porch, W. M. *Atmos. Envir.* **21,** 957–969 (1987).
9. Mandelbrot, B. B. *The Fractal Geometry of Nature* (Freeman Co., New York, 1982).
10. Samson, R. J. *et al. Langmuir* **3,** 272–281 (1987).
11. Nelson, J. A., Crookes, R. J. & Simons, S. *J. Phys.* D (submitted).
12. Meakin, P. *Phys. Rev.* A **27,** 1495–1507 (1983).
13. Botet, R. *et al. J. Phys.* A **17,** L75–L79 (1984).
14. Nelson, J. *J. mod. Opt.* (in the press).
15. World Climate Programme report WCP-55: *Report of the Experts' Meeting on Aerosols and their Climatic Effects* (eds Deepak, A. & Gerber, H. E.) (1983).
16. Weitz, D. A. *et al.* in *Scaling Phenomena in Disordered Systems* (eds Pynn, R. & Skeltorp, A.), 171–188 (Plenum, New York, 1985).
17. Hallet, J., Hudson, J. G. & Rogers, C. F. *Aerosol Sci. Technol.* **10,** 70–83 (1989).
18. Berry, M. V. *Physica D* (submitted).

The convective liquidus in a solidifying magma chamber: a fluid dynamic investigation

Geneviève Brandeis & Bruce D. Marsh

Department of Earth and Planetary Sciences, The Johns Hopkins University, Baltimore, Maryland 21218, USA

CRYSTALLIZATION at the margins of magma chambers induces strong viscosity variations[1], and recent studies[2–4] have shown how such crystallization affects the vigour of convection. Here we report an experimental study of the solidification of a layer of paraffin cooled from above. When the fluid is superheated, convection sets in at the beginning of cooling but rapidly decreases in intensity. Once the layer has lost its superheat, convection ceases and further cooling is by conduction. The interior temperature then remains constant until encountered by the upper crust. We define the convective liquidus as the temperature threshold below which convection is very weak or non-existent. In natural basaltic systems, the convective liquidus, although strictly unknown, may be very close to the true liquidus. Rapid convection may therefore not be a dominant process during the crystallization of many magma chambers; instead, convection is part of an overall intimate balance between phase equilibria, crystal growth and heat transfer.

It is essential in the experimental study of the interaction between crystallization and convection in magma chambers to choose an analogue fluid that has a melting range and no eutectic. The fluid that we used here is a mixture of pure paraffins (40% *n*-pentadecane $C_{15}H_{32}$ and 60% *n*-nonadecane $C_{19}H_{40}$), that forms a binary solid-solution in the system $C_{15}H_{32}$–$C_{19}H_{40}$ (ref. 5). It has a liquidus close to 22.6 °C and a solidus ~5–6 °C lower; the physical properties[6] are given in Table 1. The residual liquid is lighter and the crystals denser than the initial liquid. Density changes due to compositional effects over the melting range are ≤ 0.005 g cm^{-3}. Our study of the viscosity in the melting range suggests that it does not vary by more than a factor of ten until the fluid becomes non-newtonian at ~1–2 °C below its liquidus, and then the viscosity increases precipitously.

We used a 20 × 20 × 20 cm plexiglass tank with 2-cm-thick walls and bottom. The upper boundary is a 2.55-cm-thick metal plate in which water circulates under thermostatic temperature control. A comb of seven thermocouples attached to a vertical plexiglass rod in the middle of the tank provides a temperature profile normal to the roof. The calibrated thermocouples have an accuracy of ±0.2 °C. The initial temperature, T_i, in the fluid is uniform and slightly above the liquidus temperature T_L. At time $t = 0$, the metal plate is switched to the cold bath and its temperature decreases rapidly within 4 min to ~90% of the final temperature T_f. This approximates instantaneous cooling.

All the experiments performed exhibit a similar behaviour which we describe qualitatively for the experiment 45 (T_i = 24.2 °C, T_f = 17.4 °C). As cooling proceeds, the temperature of the fluid in contact with the metal plate drops, allowing the formation of a thin solid crust (<1 mm) as well as the develop-

TABLE 1 Physical properties of the paraffin mixture

Quantity	Symbol	Value
Specific heat (35 °C)	c_p	2×10^3 J kg^{-1} °C^{-1}
Density (35 °C)	ρ	0.8×10^3 kg m^{-3}
Thermal diffusivity	κ	10^{-7} m^2 s^{-1}
Thermal expansion	α	9×10^{-4} K^{-1}
Kinematic viscosity (35 °C)	ν	4×10^{-6} m^2 s^{-1}
Temperature of fusion	T_L	22.6 °C
Melting range	$T_L - T_s$	~5 °C
Heat of fusion	L_f	1.7×10^5 J kg^{-1}
Prandtl number	Pr	40

ment of the first instability at time $t \approx 1$ min. Instabilities always set in below the crust, but appear not to carry crystals deeper into the fluid. The interface between the growing crust and the liquid is planar and crystals are short (~1 mm in length) and hair-like (dendritic). At the beginning of cooling, strong convective plumes with maximum velocities of ~2 mm s^{-1} can be followed until they reach the bottom of the tank (Fig. 1*a*). Although calculation of the Rayleigh number, $Ra = g\alpha\Delta T d^3/\kappa\nu$ (where d is the total depth of the tank, κ is the thermal diffusivity, ν is the kinematic viscosity, α is the coefficient of expansion and ΔT is the temperature differential), yields $Ra = 3 \times 10^8$ for $\Delta T = 1.6$ °C, the convection is three-dimensional and unsteady but not turbulent (that is, there are no small-scale eddies and the Reynolds number is low, ~100). After two hours, convection decreases severely; maximum plume velocities are ~0.5 mm s^{-1}. Plume velocities decrease to such an extent that noticeable motion is restricted to progressively higher levels (Fig. 1*b*, *c*). After three hours, the fluid has lost nearly all of its superheat and the interior temperature is everywhere very close to the liquidus. Convection is then very sluggish (Fig. 1*c*). Note that the thickness of the crust is only ~2 cm when noticeable convection ceases whereas it takes about a further four days to crystallize the whole tank. At this stage, the fluid below the crust contains no crystals.

Temperature profiles as a function of time are shown in Fig. 2. Note that a temperature gradient is observed only in the crust and in the thin upper boundary layer. The interior temperature decreases uniformly towards the liquidus as cooling proceeds and the upper crust grows downward. As buoyancy vanishes, convection ceases. The interior then remains at the liquidus and temperature at a given depth remains constant until reached by the downward-propagating crystallization front. No significant thermal stratification is evident at any time. The temperature at which convection becomes very weak or non-existent is defined here as the 'convective liquidus' and has been found to be equal to the thermodynamic liquidus, within the accuracy of the measurements, regardless of the initial amount of superheat. This is the first critical feature of these experiments. The existence of a convective liquidus holds regardless of the cooling geometry, as we have also performed experiments on the cooling along a vertical side wall.

Figure 3*a* is a plot of temperature against time at different depths for experiment 47 which is similar to 45 but has a longer data set. Two stages can be distinguished: 'active' convection (stage I), where the interior temperature rapidly decreases to the liquidus, which is followed by stage II where cooling proceeds essentially by conduction and the interior temperature remains at the liquidus. The second critical point in these experiments is that the duration τ of stage I is very short compared with the total solidification time or the duration of stage II (Fig. 3*a*). The duration of stage I depends on the amount of superheat $\Delta T = T_i - T_L$ and the thickness of the tank. It can be calculated using the formula given in ref. 7:

$$\tau = \left(\frac{14.3\, d^2}{\kappa}\right) \mathrm{Ra}^{-1/3} \qquad (1)$$

where the Rayleigh number is based on the whole tank depth d; τ is equal to 124 min in the case of experiment 47 and represents ~4% of the total conductive solidification time (Fig. 3*a*). On the other hand, quiescent stage II cooling is closely approximated by conduction only, in agreement with other studies[8]. It is during stage II that the principal crystallization of the tank takes place. Finally, at times $t > 12$ h, crystals start to form on the bottom and the sidewalls, because of unavoidable wall and floor cooling. This produces some evolution of the liquid composition during the crystallization of the whole tank and may explain the departure of the interior temperature from the liquidus at depth $z = 9.8$ cm after $t = 14$ h (Fig. 3*a*).

Before extrapolating the results of the present experiments to

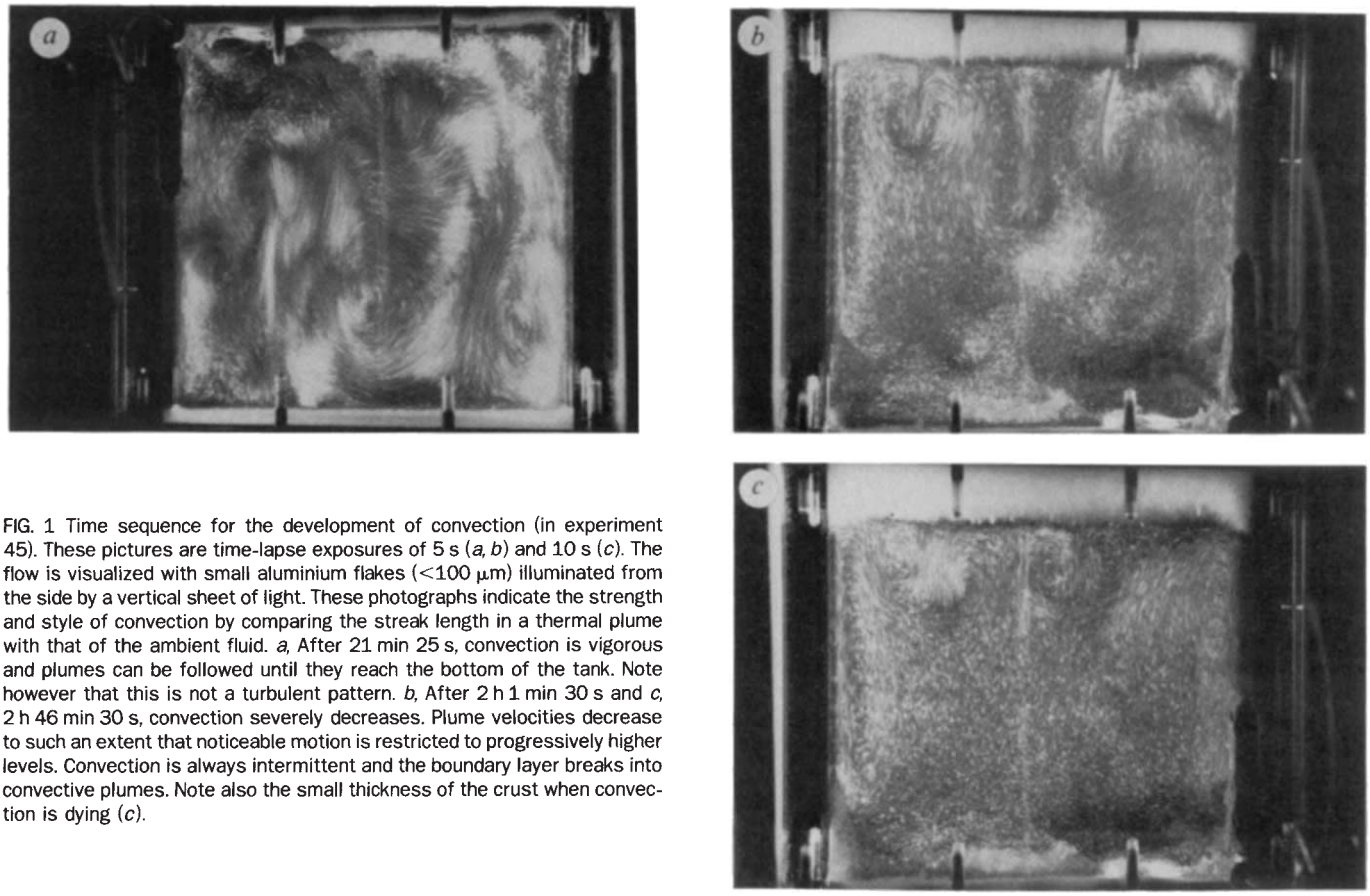

FIG. 1 Time sequence for the development of convection (in experiment 45). These pictures are time-lapse exposures of 5 s (*a*, *b*) and 10 s (*c*). The flow is visualized with small aluminium flakes (<100 μm) illuminated from the side by a vertical sheet of light. These photographs indicate the strength and style of convection by comparing the streak length in a thermal plume with that of the ambient fluid. *a*, After 21 min 25 s, convection is vigorous and plumes can be followed until they reach the bottom of the tank. Note however that this is not a turbulent pattern. *b*, After 2 h 1 min 30 s and *c*, 2 h 46 min 30 s, convection severely decreases. Plume velocities decrease to such an extent that noticeable motion is restricted to progressively higher levels. Convection is always intermittent and the boundary layer breaks into convective plumes. Note also the small thickness of the crust when convection is dying (*c*).

natural systems, it is necessary to understand the structure of the unstable part of the boundary layer[9-12], where the viscosity changes as a result of the gradients of temperature, composition and crystal content. First, there might be some important compositional effects in the boundary layer. Note, however, that the chemical diffusivity, although strictly unknown, is usually much smaller than the thermal diffusivity, and that compositional effects do not become significant before the cessation of thermal convection (Fig. 3*a*). As cooling proceeds, compositional effects might become important in stifling convection, but this is also the case in magmas. In terms of the effect of crystal content, some crystals might be carried by convection into the interior, especially if the crystallization timescale is long relative to the timescale of convective instability[2]. No crystals were observed in the unstable boundary layer, which may imply that crystallization is rapid compared with convective instability. This could, however, also be because nucleation is heterogeneous and the crystals form an interconnected dendritic network that cannot take part in the unstable boundary layer.

The paraffin properties are, however, different from those of magmas (Table 1) so how do our results relate to magmatic systems? For paraffin, the Prandtl number, Pr, is 40 and $Ra > 10^8$, so convection could possibly take a different form from that in magmas[13], where Pr is larger. Nevertheless, no turbulence was ever observed. The Stefan number $\sigma = c_p \Delta T / L$ is >0.1 but less than that in magmas, thus the heat released at the interface is affected only slightly during the propagation of heat through the crust[14]. However, a larger σ could be obtained by fixing T_f at a lower value, without changing the results. In magmas, the density changes arising from compositional effects are usually larger than thermal changes, unlike the paraffins used here. However, there is no chemical evolution without crystallization. Crystallization requires some cooling and it is essential to study the thermal regime. We therefore suggest that a similar behaviour could be observed in natural systems, where the residual liquid is light. Vigorous convection would seem possible until the magma reached a prohibitively high viscosity as a result of increasing crystallinity, which might occur after ~50% crystallization[15]. However, this critical crystallinity is bound to be dependent on the strain rate of convection. We need to discover the degree of crystallinity at which magmatic convection ceases.

Crucial information on this issue comes from the thermal history of Hawaiian lava lakes[16-21], formed by eruptive filling of pit craters 15–120 m deep. Phenocrysts in the initial magma settled out, leaving the body at its liquidus temperature, and the central temperature remained relatively close to the liquidus until crystallization fronts reached the centre. The shape and evolution of the natural vertical temperature profiles are strikingly similar to those observed in these experiments (compare our Fig. 2 with Figs 7 and 8 in ref. 20). Figure 3*b* represents the data for the estimated central temperature in the lava lakes

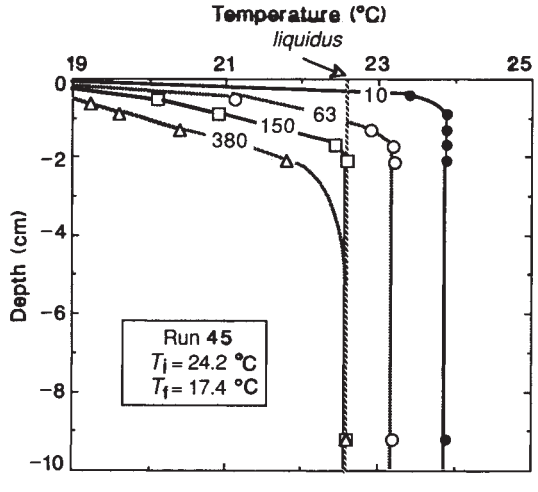

FIG. 2 Vertical profiles for the interior temperature at different times (experiment 45). Time is indicated in minutes along the curves. The thermal gradient is restricted to the solid crust and a thin boundary layer. Temperature is uniform in the interior. At a given depth in the interior, temperature decreases only to the liquidus (22.6 °C) and is then locked to this temperature until the crust encounters this point.

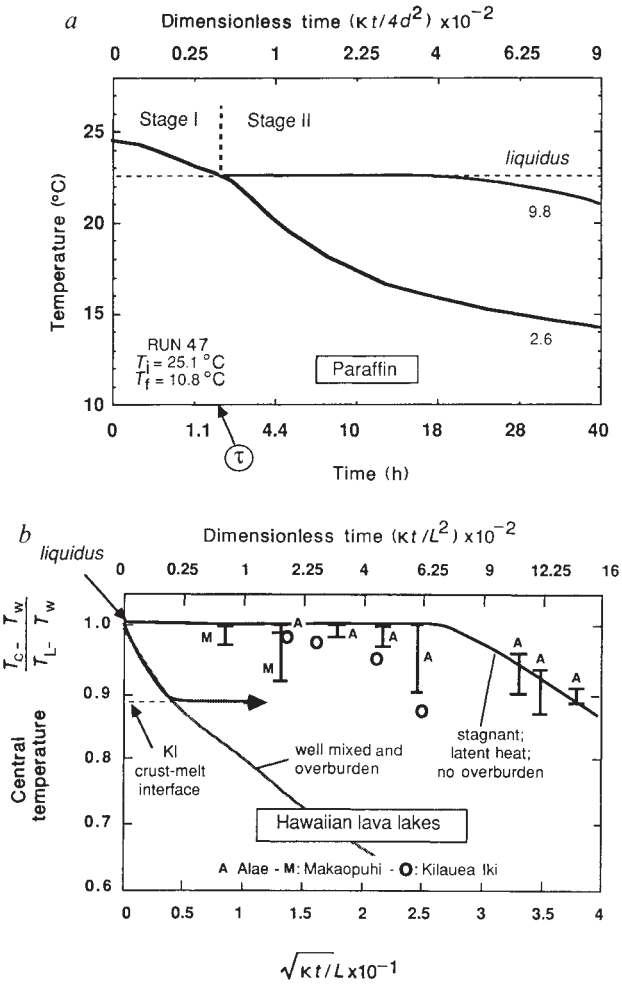

FIG. 3 *a*, Temperature versus time at different depths (indicated in cm under the curves) (experiment 47). The depth $z = 2.6$ cm is completely within the crust after $t = 2$h, whereas $z = 9.8$ cm remains at the liquidus. The scale is linear in $\sqrt{t}$. Dimensionless time $t^* = \kappa t/4d^2$ is also given as a scale for comparison with a body of thickness L cooled from above and below. Two stages can be distinguished. For $t^* < \tau$ or $t < 0.005$, cooling proceeds uniformly in the whole tank by convection (stage I). For larger times $t > \tau$, cooling proceeds mainly by conduction (stage II). Interior crystallization starts only when encountered by the growing crust. *b*, Variation in central temperature with dimensionless time $t^* = \kappa t/L^2$ during cooling from above and below of a layer of thickness L for two extreme cooling models. The first (upper curve), assumes the minimum rate of heat transfer (as calculated in ref. 4, assuming no convection, no overburden and taking into account the effect of latent heat). The second (lower curve) assumes the maximum rate of heat transfer (obtained for a perfectly well mixed model[29] where temperature decreases uniformly with time throughout the layer). The data and error bars correspond to estimated temperatures in the interior during solidification of Hawaiian lava lakes (refs 4, 16–20 and R. T. Helz, personal communication). Dimensionless times and temperatures are calculated assuming $\kappa = 10^{-6}$ m^2 s^{-1}, $T_w = 0$ °C, $L = 13.7$ m and $T_L = 1,150$ °C for Alae, $L = 83$ m and $T_L = 1190$ °C for Makaopuhi, $L = 120$ m and $T_L = 1,200$ °C for Kilauea Iki. Also indicated by the curve with the arrow is the thermal evolution of Kilauea Iki, assuming that rapid convection continues until reaching the temperature of the crust–melt interface for which crystallinity is ~50% (ref. 18).

as well as the temperature evolution calculated assuming two extreme cooling models (see Fig. 3 legend). The thermal histories of the lava lakes are closer to the conductive curve representing stagnant magma. Temperatures in Kilauea Iki depart from the ideal conduction model after $t^* \sim 0.0225$, which may be due to such observed processes as diapiric transfer of melt, crystal settling or gas exsolution[18]. However, there is no significant decrease of the interior temperature at early times, after the main degassing event ($t^* \approx 0.0045$; ref. 21 and M. Mangam, personal communication) or even after its complete cessation ($t^* \approx 0.013$). Comparison of the experimental (Fig. 3*a*) and the observed thermal (Fig. 3*b*) histories shows a remarkable similarity in terms of the temporal constancy of the interior temperature. This suggests the existence of a convective liquidus in the lava lake that is apparently near the actual magmatic liquidus itself. We suggest that it might not be the exsolution of gas that impedes convection[17], but the advancement of the growing crust which partitions from the magma the buoyancy necessary for convection.

In a closed system, although convection may be vigorous at the beginning of cooling and may be able to carry crystals into the interior and evacuate the large amount of latent heat released by the crystallization, its intensity soon diminishes. Kinetic effects are important in cooling magmas, as has been stressed in numerical modelling[22]. This is confirmed by recent observations[23,24] that crystallization of plagioclase in the Makaopuhi lava lake takes place at an undercooling of $<10^{-1}$ °C. The present experiments suggest that a thermal equilibrium will be achieved and the convective liquidus will be locked to the liquidus itself. They also show that, once the convective liquidus is reached, convective cooling may be negligible. This may also explain the results of studies[4,25] that show that the solidification of lava lakes can be modelled by conductive cooling only, in contrast to previous experiments that do not involve a convective liquidus[7,26,27] and calculations that assume turbulent convective cooling[7,27,28].

We therefore suggest that these results may hold for magma chambers evolving as closed systems, where the upper crust develops and the residual liquid is lighter than the original magma. In such chambers intruded at the liquidus, convection is apt to be sluggish and the interior temperature remains at the convective liquidus until being encountered by the growing crust. In magma chambers intruded with some initial superheat, the period of rapid convection will be short compared with the total solidification time (5 years compared with ~3,000 for a 1 km-deep basaltic chamber, intruded with a ΔT of 10 °C). Subsequently the interior temperature remains at this convective liquidus, which is close to the liquidus itself. This rapid loss of superheat may explain the well-known absence of superheated magmas in the near-surface environment. We suggest that, to a good approximation, the initial period of rapid convective cooling can be ignored and overall the solidification history of many magma chambers can be adequately modelled by conduction only. □

Received 12 October 1988; accepted 8 May 1989.

1. McBirney, A. R. & Murase, T. *A. Rev. Earth planet. Sci.* **12,** 1–10 (1984).
2. Brandeis, G. & Jaupart, C. *Earth planet Sci. Lett.* **77,** 345–361 (1986).
3. Smith, M. K. *J. Fluid Mech.* **188,** 547–570 (1988).
4. Marsh, B. D. *J. Petrol.* (in the press).
5. Turner, W. R. *Ind. Engng Chem. Prod. Res. Develop.* **10,** 238–260 (1970).
6. Humphries, W. R. & Griggs, E. I. *NASA tech. Rep.* **1074** (Science and Technology Information Office, Baltimore–Washington Airport, Baltimore, 1977).
7. Jaupart, C. & Brandeis, G. *Earth planet. Sci. Lett.* **80,** 183–199 (1986).
8. Viskanta, R. in *Solar Heat Storage: Latent Heat Materials* Vol. 1 (ed. Lane, G. A.) 153–222 (CRC, Boca Raton, Florida, 1983).
9. Strengel, K. C., Oliver, D. S. & Booker, J. R. *J. Fluid Mech.* **120,** 411–433 (1982).
10. Richter, F. M., Nataf, H. C. & Daly, S. F. *J. Fluid Mech.* **129,** 173–192 (1983).
11. Morris, S. & Canright, D. *Phys. Earth planet. Inter.* **36,** 355–373 (1984).
12. Jaupart, C. & Parsons, B. *Phys. Earth planet. Inter.* **39,** 14–32 (1985).
13. Krishnamurti, R. *J. Fluid Mech.* **42,** 205–307 (1970).
14. Ozisik, M. N. *Heat Conduction* (Wiley, New York, 1980).
15. Marsh, B. D. *Contr. Miner. Petrol.* **78,** 85–98 (1981).
16. Peck, D. L. *Prof. Pap. US geol. Surv.* **935-B** (1978).
17. Wright, T. L. & Okamura, R. T. *Prof. Pap. US geol. Surv.* **1004** (1977).
18. Helz, R. T. in *Magmatic Processes: Physico Principles* Spec. Publn 1 (ed. Mysen, B. O.) 241–258 (Geochemistry Society, 1987).
19. Helz, R. T. & Thornber, C. R. *Bull. volcanol.* **49,** 651–668 (1987).
20. Helz, R. T. *Geol. Soc. Am. Bull.* **101,** 578–594 (1989).
21. Mangam, M. T. & Helz, R. T. *Eos* **66,** 1133 (1985).
22. Brandeis, G., Jaupart, C. & Allègre, C. J. *J. geophys. Res.* **89,** 10161–10177 (1984).
23. Cashman, K. V. & Marsh, B. D. *Contr. Miner. Petrol.* **99,** 292–305 (1988).
24. Maaløe, S. *Am. J. Sci.* (submitted).
25. Peck, D. L., Hamilton, M. S. & Shaw, H. R. *Am. J. Sci.* **277,** 415–437 (1977).
26. Jaupart, C., Brandeis, G. & Allègre, C. J. *Nature* **308,** 535–538 (1984).
27. Turner, J. S., Huppert, H. E. & Sparks, R. S. J. *J. Petrol.* **27,** 397–437 (1986).
28. Huppert, H. E. & Sparks, R. S. J. *Contr. Miner. Petrol.* **75,** 279–289 (1980).
29. Carslaw, H. S. & Jaeger, J. C. *Conduction of Heat in Solids* (Clarendon Press, Oxford, 1959).

ACKNOWLEDGEMENTS. We thank Mark Smith and George Bergantz for discussions, Rosalind Helz and Margaret Mangam for discussions on the Hawaiian lava lakes, and Alexander McBirney and Steve Tait for their reviews. This work is supported by the NSF, NASA and IPGP (France).

Acoustic emissions and shear instabilities during phase transformations in Si and Ge at ultrahigh pressures

Charles Meade & Raymond Jeanloz

Department of Geology and Geophysics, University of California, Berkeley, California 94720, USA

ACOUSTIC emissions are commonly observed at low pressures as they are characteristic of brittle deformation[1,2]. Most solids are ductile above a few gigapascals (GPa), and acoustic emissions have not been recorded from solids above 5 GPa. Here we describe acoustic emissions and shear instabilities that are associated with the β-Sn → simple-hexagonal phase transformation in Si and Ge to pressures as high as 70 GPa, well above the brittle–ductile transitions of both elements. We propose that the events are driven by rapid atomic motions across displacive phase transformations, and not by fracturing or cracking of the samples. These phenomena may be relevant to the processes that generate deep-focus seismicity in the Earth's mantle.

We compressed powdered Si and Ge (grain size 1–3 μm) without a pressure medium in a Mao–Bell diamond cell[3] at room temperature. Less than 5% by volume of ruby powder (grain size ≤3 μm) was placed at the interface between the sample and the upper diamond, and the pressure was measured with the ruby fluorescence technique[4]. We determined the shear stresses in each run by measuring pressure gradients across the sample[5], and we observed the sample deformation visually with an optical microscope.

Previous studies have documented brittle deformation in Si and Ge to confining pressures of 5 GPa at room temperature[6]. When compressing samples of Si and Ge from zero pressure, we find that this brittle, stick-slip deformation appears as sudden shearing within small regions of the sample accompanied by rapid changes in the stress birefringence of the diamonds. These visual observations indicate that the brittle–ductile transition occurs at pressures close to the diamond → β-Sn phase transformation in Si and Ge at room temperature (~9 GPa; refs 7–9). This particular phase transformation involves a considerable volume change ($\Delta V/V > 0.17$), and is always associated with large amounts of ductile deformation distributed over the entire sample.

As we compress Si through the β-Sn → simple hexagonal transformation ($P \approx 16$ GPa; refs 7, 8), we observe sudden, brittle-like deformation at pressures well above the brittle–ductile transition. At the transformation pressure, the polycrystalline silicon produces large acoustic emissions that we can visually correlate with rapid displacements through the sample over lengths of ~50 μm (Fig. 1). The abrupt nature of these instabilities resembles the brittle deformation that we observe at lower pressures, but it is unusual given the relatively low